Icarus **149**, 384–396 (2001)
doi:10.1006/icar.2000.6528, available online at http://www.idealibrary.com on IDEAL®

Saturn's E Ring and Production of the Neutral Torus

S. Jurac

Massachusetts Institute of Technology, MIT 37-662b, Cambridge, Massachusetts 02139; and University of Virginia, Engineering Physics, Thornton Hall 103, Charlottesville, Virginia 22903
E-mail: jurac@space.mit.edu

R. E. Johnson

University of Virginia, Engineering Physics, Thornton Hall 103, Charlottesville, Virginia 22903

and

J. D. Richardson

Massachusetts Institute of Technology, MIT 37-662b, Cambridge, Massachusetts 02139

Received November 29, 1999; revised August 7, 2000

Recent Hubble Space Telescope (HST) observations of the densities of neutral OH molecules that coexist with and are precursors of the plasma ions have constrained models for the plasma sources. An orbital simulation model of the evolution of H_2O molecules emitted from the satellites and the E ring is employed to put additional constraints on the possible plasma/neutral sources in Saturn's magnetosphere. We find that a large H_2O source concentrated near the orbit of Enceladus (of the order 10^{27} H_2O molecules/s) is needed to account for the observed OH neutral cloud. We suggest that a large amount of optically unobserved material near Enceladus could provide the "missing" H_2O source. A Monte-Carlo collisional transport code for sputtering of ice surfaces is developed and applied to the E-ring grains. Grain lifetimes are found to be short ($\sim$50 years for 1-μm grains and only a few years for 0.1-μm grains), so grains must be resupplied regularly to keep the E ring in the present state. Orbital collisions between icy fragments, possibly remains of a disrupted satellite near Enceladus, are the suggested mechanism for replenishing the E ring.

Key Words: **magnetospheres, planetary rings, saturn; ices, Saturn; magnetosphere, satellites of Saturn.**

1. INTRODUCTION

The E ring is a diffuse, tenuous ring of micrometer-size ice grains, which extends over a larger region than any other known planetary ring. This ring has a sharp inner edge between Mimas and Enceladus, expands azimuthally in latitude as it crosses the orbits of Tethys and Dione, and fades away beyond Rhea's orbit. The ring peaks at and appears to emanate from Enceladus; the peak is coincident with the densest region of Saturn's OH neutral torus. This unique environment, which provides an excellent test for models of charged-grain dynamics and dust–plasma interactions, has initiated a number of recent modeling efforts (e.g., Horanyi *et al.* 1992, Hamilton and Burns 1994, Dikarev 1999). Renewed interest in the E ring was stimulated by the exciting discovery by Hubble Space Telescope (HST) of a neutral OH torus (Shemansky *et al.* 1993, Hall *et al.* 1996, Richardson *et al.* 1998) and by the launch of Cassini spacecraft, which will make many passes through the E ring. Because this ring is imbedded in the plasma trapped in Saturn's magnetosphere (Krimings *et al.* 1983, Lazarus and McNutt 1983, Richardson and Sittler 1990) the E-ring grains are eroded by the plasma in a process called sputtering. Here we examine this process as a possible source of the OH neutrals that, roughly, coorbit with the E-ring grains.

Pang *et al.* (1984) contended that the observed "blue" E-ring spectrum is most consistent with a narrow size grain distribution, containing grains 1–1.25 μm in radius. Contrary to this "uniform-size" distribution, other known rings exhibit an inverse-power-law grain-size distribution, which is the distribution that is expected from a collisional disruption process. In addition to the main Saturnian rings, a power-law distribution characterizes the G ring, which is spatially closest and most similar to the E ring (Throop and Esposito 1998). Showalter *et al.* (1991) conducted a comprehensive study of all existing measurements of the E ring and found that none of the power-law distributions used is consistent with the data, and that a narrow, micrometer-size grain distribution appears to provide the best match. Most recently, Nicholson *et al.* (1996) also found that the spectrum has the best agreement with a narrow particle-size distribution with mean grain sizes between 0.3 and 3 μm. However, their spectrum was less blue, providing latitude for a broader grain-size distribution.

Noise recorded by the Voyager 1 planetary radio-astronomy experiment (Meyer-Vernet *et al.* 1996) and plasma-wave

0019-1035/01 $35.00

experiment (Tsintikidis *et al.* 1995) was used to infer the particle sizes at 6.1 R_s. Both studies detected the dust peak southward (by about 0.1 R_s) of the equatorial plane, and Tsintikidis *et al.* (1995) suggested that this dust may be either part of the E ring or a localized ringlet associated with Dione. Meyer-Vernet *et al.* (1996) gave 1 μm as their best guess for the particle radii, assuming a particle concentration given by the model of Showalter *et al.* (1991). Tsintikidis *et al.* (1995) found $\lesssim$5-μm ice particles as the source of noise, but those authors suggest that multiple impacts of smaller particles could also be responsible for the measured signal (the instrument detection threshold was above 0.7 μm). The Voyager 2 PLS (Plasma science experiment) and PRA instruments also recorded noise during the passage through the nearby G ring at 2.9 R_s (Gan-Baruch *et al.* 1994, Tsintikidis *et al.* 1994). Tsintikidis *et al.* (1994) estimated particles sizes of $\sim$10 μm and noted that if the instrument was able to detect all particles (i.e., those below the instrument threshold) the total impact density would be larger, yielding smaller particle radii.

A new exciting observation of a bright arc of particles orbiting Saturn (Roddier *et al.* 1998) might shed light on the existing features and origin of the E ring. A rapidly expanding cloud, seen in the vicinity of Enceladus' orbit, disappeared in a matter of hours. This cloud, consisting presumably of small grains, was likely produced by a collision between orbiting icy objects (Roddier *et al.* 1998). Based on its rapid disappearance, as discussed later, we believe that this cloud was predominantly composed of submicrometer particles.

Additional clues for a possible submicrometer E-ring grain population come from orbital dynamics calculations. Hamilton and Burns (1994) simulated E-ring particle dynamics including collisions between E-ring grains and satellites. Their simulation yielded a significant population of small submicrometer grains. Horanyi *et al.* (1992) modeled the E-ring particle dynamics and showed that 1-μm charged grains launched from Enceladus would spread more rapidly than smaller or larger grains. Although this mechanism could be responsible for many of the observed E-ring features, Horanyi *et al.* (1992) contend that this process would not be able to filter the initial power-law distribution and maintain a narrow, nearly uniform-size distribution in its collisional environment. Dikarev (1999) included the plasma drag force in the orbital dynamics calculation and showed that submicrometer grains would drift outward faster and spread out more rapidly than previously thought, but still not fast enough to produce a uniform-size population (Dikarev 1999, private communication).

Finally, evidence for a large apsorbtion area near Enceladus, which cannot be accounted for by the optical observations, comes from Paranicas and Cheng (1997). Based on Voyager 2 observations of satellite signatures in the energetic particle population, they found that an object 25 times the absorbing area of Enceladus is needed in its vicinity to account for an observed micro-signature.

Here we investigate the sputtering of ice grains, a process that preferentially erodes submicrometer grains, and examine its implications for existing E-ring models. We calculate both the ion and neutral mass flux to the charged E-ring grains and show that grains smaller than $\sim$1 μm are eroded preferentially, depleting the submicrometer grain population. In addition, we calculate the supply rates to the neutral torus by sputtering of E-ring grains. The sputtered molecules are tracked until ionized, and the resulting neutral cloud is compared with the observed OH cloud (Richardson *et al.* 1998, Richardson 1998). We conclude that the existence of a large population of submicrometer-sized grains in the E ring would be consistent with observational evidence. Before carrying out the new calculations, we briefly review the models for the sources of the plasma and neutral torii.

1.1. Sources of Neutrals

The source of heavy ions, presumably O^+, in Saturn's inner magnetosphere has been a topic of considerable interest since the Pioneer and Voyager spacecraft discovery of this plasma. Based on the Voyager measurements of the spatial distribution of the plasma at Saturn, there has been debate on the importance of the satellites and E ring as sources. Most recently, the spatial overlap of the E ring with the heavy plasma torus was suggestive to Morfill *et al.* (1993), Hamilton and Burns (1994), and Ip (1997) that the E ring might be a source of the plasma. This plasma is formed from water molecules that are dissociated and ionized, producing the heavy ion component of the plasma (Richardson *et al.* 1998). Morfill *et al.* (1993) proposed self-sputtering of the E ring as a source of the plasma cloud. On the other hand, Hamilton and Burns (1994) suggested that charged micrometer-size E-ring grains, which over time develop orbits with large eccentrities, collide with Enceladus and other satellites ejecting a sufficient amount of vapor to account for the neutral production rates (Hamilton and Burns, 1993).

Early estimates of the relative source strengths of neutral water molecules sputtered from the E-ring grains, from the surfaces of the icy satellites, or from particles in the main rings indicated that both Enceladus and the E ring were not very important sources (e.g., Johnson *et al.* 1989). Rather, $>$10 keV plasma-ion sputtering of the large icy satellites Tethys, Dione, and Rhea (Cheng and Lanzerotti 1978, Eviatar 1984, Johnson *et al.* 1989) and micrometeorite vaporization of the main ring particles (Pospieszalska and Johnson 1991) were proposed as the dominant sources. However, the direct observation of neutral OH (Shemansky *et al.* 1993) gave an OH concentration in the ring plane of 170 cm^{-3}, much larger than predicted. Recently, Richardson *et al.* (1998) considered the HST OH observations and developed a 2-D plasma/neutral model. Their neutral densities peak close to Enceladus, where the E-ring density is maximum, with a total neutral density of over 1200 cm^{-3}. They also found that the total neutral source rates needed to maintain water-like neutrals in this region are at least an order of magnitude larger than the source rates given by Shi *et al.* (1995) based on sputtering of satellites and the E ring. Although this model is

not yet fully self-consistent, it provides the strongest evidence that more robust sources are needed.

Because the source of water products from sputtering of both the icy satellites and the E-ring appears too small to explain the density of neutrals, we examine possible enhancements to the sputter-produced flux. These calculations require a reexamination of the sputter-flux produced from an individual grain and a reexamination of the grain-size distribution. We show that the total surface area of the E ring might be much larger than inferred from the direct optical observations and that the missing neutral/plasma sources could be accounted for by sputtering of small grains that are resupplied from an active source.

2. SPUTTERING OF WATER–ICE SURFACES

Plasma ions entering a material collide with the constituent atoms, initiating a cascade of collisions. This results in the ejection of atoms and molecules into the gas phase, a process called sputtering. A schematic diagram of this process is shown in Fig. 1. For a flat surface, indicated by the dashed line, an incident ion (thick arrow) collides with target atom and creates recoils (thin arrows), which in further collisions produce new generations of recoils, and so on. Finally, when a recoil leaves the target surface sputtering occurs (indicated by "a" in Fig. 1). The sputtering yield is then given as a number of sputtered atoms per incident particle.

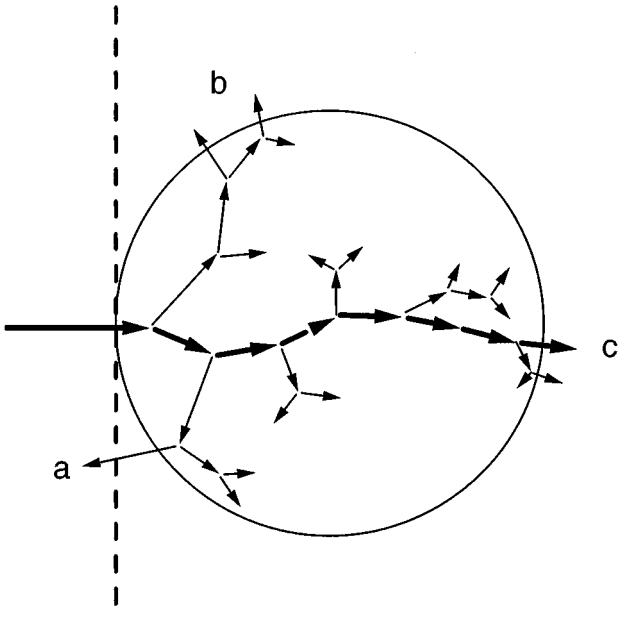

FIG. 1. Schematic diagram of the cascade of collisions produced by ion or atom on a material. As an incident ion collides with target atoms, it slows down and produces a recoil-cascade. When one of the recoils is set in motion in the surface layer with an energy greater than its binding energy and in the direction of escape, it is ejected from the solid (a). For a spherical target sputtering is enhanced due to more recoils reaching the surface. Grains are mainly destroyed by sideward (b) sputtering and then finally by sputtering from the back surface of a grain (c).

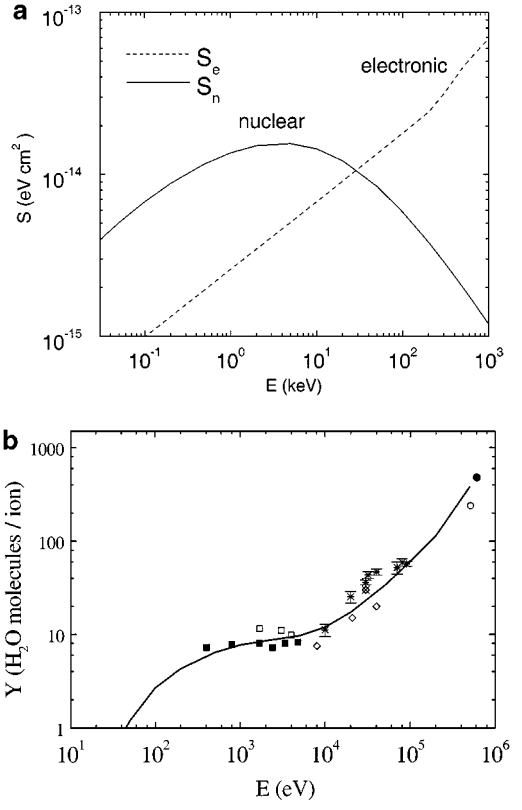

FIG. 2. (a) The electronic and nuclear stopping cross sections S_e (dotted line) and S_n (solid lines) versus incident O energy for H + 2O tabulated by SRIM 98. The figure shows that the nuclear cross section is larger at lower energies, while for the higher energies, the electronic stopping cross section dominates. (b) Measured sputtering yield for water–ice at normal incidence for semi-infinite target versus incident O ion energy. Line indicates our model, while symbols represent the compilation of the laboratory measurements of the sputtering yield given by Shi *et al.* (1995).

Sputtering of ice is determined by the energy deposited by the incident ion. It occurs in response to both the momentum transfer and electronic excitations and ionizations produced near the surface of the solid. Therefore, for an ion incident on a solid, the energy lost per unit path length in the solid, dE/dx, is due to momentum transfer to the atomic constituents, $(dE/dx)_n$ (called elastic nuclear or "knock-on" collisions), and due to ionization and excitation of the molecules, $(dE/dx)_e$ (e.g., Johnson 1990). The total sputtering yield, Y, is often written as a sum of nuclear and electronic contributions, $Y \approx Y_n + Y_e$. For ion bombardment of an ice, electronic sputtering (Y_e) is the dominate contribution at high velocities and collisional, knock-on, sputtering (Y_n) dominates at low incident velocities. As an illustration Fig. 2a shows nuclear and electronic cross sections for O^+ incident on H_2O based on a model given by Ziegler *et al.* (1985). The nuclear cross section S_n (solid line) is larger at low energies, while for energies above ~30 keV the electronic cross section, S_e, dominates.

In the nonlinear sputtering regime, which applies for ices and condensed gases, Y_e is found to be roughly proportional to $(dE/dx)_e^2$. This dependence is consistent with the "thermal

spike" model for sputtering (Gibbs *et al.* 1988, Johnson 1990), although the thermal spike model has been questioned recently (Bringa *et al.* 1999a, 1999b). Here we model the sputtering from ice surfaces, accounting for both knock-on sputtering and the electronically induced sputtering.

2.1. Sputtering Model

To calculate knock-on sputtering we used a Monte Carlo binary collision transport code, which calculates the trajectory of an energetic ion or atom penetrating a material. Our program principally follows the code known as TRIM (TRansport of Ions in Matter) developed by Ziegler, Biersack, and Littmark at IBM Research (Ziegler *et al.* 1985) and described by Eckstein (1991). Each incident particle starts with a given energy, position, and momentum and its trajectory is followed in the target, collision by collision, until it loses so much energy that it can no longer displace other atoms or it leaves the target surface. A knock-on collision with a target atom, described by a repulsive interaction potential, initiates a sequence of collisions producing recoil atoms, whose paths are also tracked (Fig. 1).

In our calculation the "Universal" or "ZBL-potential" is used (Ziegler *et al.* 1985) to describe the momentum transfer between an energetic atom and a stationary atom in the solid. The target structure is assumed to be amorphous in this model. That is, there is no periodic structure, so the next collision partner is found by a random selection process. The distance between collisions is assumed to be the mean spacing of atoms in the solid and the impact parameter for each collision is then chosen by a Monte Carlo procedure. The scattering angle and energy transfer to the recoil from a collision are found from the interaction potential using a parametrized analytic formula (so-called MAGIC formula, Ziegler *et al.* 1985) for a given incident particle energy, impact parameter, and distance of closest approach. Due to their smaller mass, incident H^+ ions are not nearly as efficient as O^+ in transferring their energy collisionally, so the H^+ contribution to the net sputtering rate is small. On the other hand, the H atom contribution to the stopping power of H_2O is not negligible, and the total nuclear and electronic cross sections for H_2O used here is a sum of O and H cross sections. Because we calibrate the calculations to the data, we have treated water molecules in the transport code as single entities with mass 18 and atomic number 10. This was found to be a more appropriate choice at lower energies with only a minor impact at larger energies, where the electronic component dominates the sputtering yield (Fig. 2a). This approach implies that the water molecule is sputtered as a whole, consistent with measurements, and not as three separate atoms ($2H + O$). Our approach accurately describes penetration of the ions into ice, with penetration depths within 10% of those tabulated by SRIM.

The code was previously developed and applied to interstellar grain destruction (Jurac *et al.* 1998) and was modified here to model the electronic sputtering of ice. The nuclear contribution to the sputtering yield, Y_n, was obtained as a direct output from the collisional transport code using an empirical fit for the effective surface binding energy with spherical binding condition. A more detailed description of the code and the underlying assumptions with an application to both planar and spherical targets was given by Jurac *et al.* (1998). To obtain the ejection, the electronic cross section was used to calculate the electronic energy deposited by the incident ion and all recoils in a 5-Å surface layer, corresponding roughly to the first two surface monolayers of target material. The electronic sputtering yield Y_e was then assumed to be proportional to $(dE/dx)_e^2$. This "quadratic sputtering regime" is found to be valid for water below 100 K (e.g., Brown *et al.* 1982, Johnson, 1990). The total sputtering yield for a flat surface at normal incidence was calculated as a sum of electronic Y_e and nuclear Y_n yields, calibrated to provide the best fit to the laboratory measurements for a flat surface (i.e., semi-infinite target). Our code follows all recoils, not only those energetic enough and close enough to surface to induce sputtering in semi-infinite targets, which is necessary for small spherical targets. By following a large number of the recoils meaningful statistics were obtained for a number of grain sizes and for energies up to 200 keV.

Figure 2b shows the compilation of the laboratory measurements of the temperature independent part of the sputtering yield for water ice vs incident energy (Shi *et al.* 1995). Below ~100 K, the temperature region of interest for the E-ring grains, the temperature-dependent contribution to the yield is small and is ignored here. Also shown is our fit to the data using the described model (solid line) for incident O^+ ions. Our model for normal incidence is in agreement with the measured yield for the dominant sputtering energies of interest in Saturn's magnetosphere, between 1 and 100 keV. Agreement degrades at energies of the order of a few hundred electron volts, possibly due to the uncertainties in the nuclear cross sections and the yield measurements or to chemical changes in H_2O that are not described by the model.

As an example, Fig. 3 shows the enhancement in the sputtering yield vs incident angle, $Y(E, \theta)/Y(E, 0)$, for energies of 1 keV (dashed) and 200 keV (solid). These are compared to the measured yield for He^+ on CO at 1.5 MeV (crosses, Brown *et al.* 1984), all normalized to the sputtering yield at normal incidence. A fit to the 1.5-MeV measurements given by Johnson (1990) as $\cos(\theta)^{-1.6}$ is also plotted in the same figure (dotted). At larger incident angles the recoil cascades occur closer to the surface, resulting in a larger yield.

Also, as the incident ion energy increases, recoils from deeper layers are able to reach the surface resulting in a larger enhancement for larger energies. Although no measurements exist for the relevant energy range or for water–ice, our model for 200-keV ions approaches the He^+ on CO measurements data obtained at 1.5 MeV.

If θ is the incident angle and $Y(E, \theta)$ is the yield as a function of angle, the average sputtered flux integrated over all angles at a given energy is given for isotropic incidence as

$$\langle Y(E, \theta)\rangle_\theta = 2\int_0^{\pi/2} Y(E, \theta)\sin(\theta)\cos(\theta)\, d\theta. \qquad (1)$$

The resulting yield, as seen in Fig. 4, which is twice the yield for

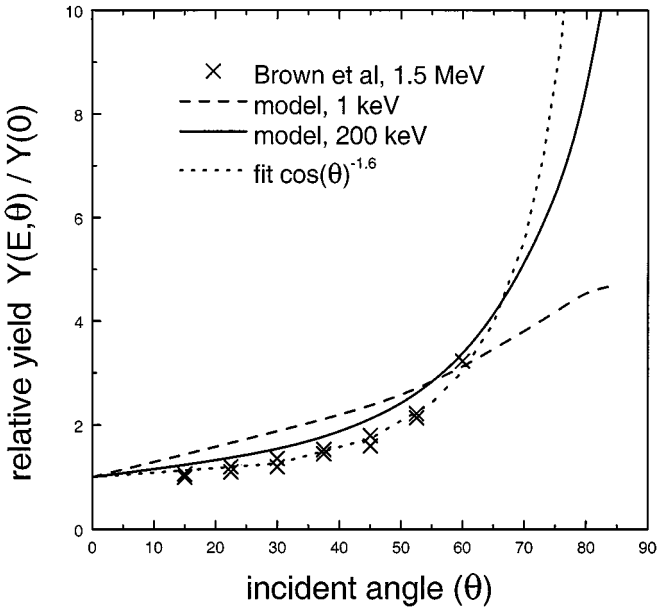

FIG. 3. Modeled sputtering yield for water–ice vs incident angle on a semi-infinite surface. Our model for energies 1 keV (dotted) and 200 keV (dashed) and measured yield for He on CO at 1.5 MeV (crosses, Brown *et al.* 1984), all normalized to sputtering yield at normal incidence. Dotted line represents an empirical fit to the data, $\cos(\theta)^{-1.6}$, previously assumed as the correct angular yield dependence for all energies.

normal incidence at ∼100 eV and ∼2.5 times the yield at 2 keV, slowly increases at larger energies. These enhancements are all smaller than that estimated earlier (∼4, Shi *et al.* 1995) based on the mega electron volt ion data. The calculated enhancements are applicable to smooth flat surfaces bombarded by isotropic plasma, like large grains in planetary plasmas, that is, whenever the ion penetration depth is small compared to the size of the body.

2.2. Sputtering of Small Grains

When the penetration depth of the incident particle becomes comparable to the grain size, sputtering increases in comparison to the semi-infinite (planar) target. The incident ion initiates a cascade of recoil atoms in the material and for a small grain the energetic recoils are more likely to reach the surface and induce sputtering ("b" in addition to "a" in Fig. 1). Surface curvature starts to play a role even when the penetration depth of an incident ion is a fraction of the grain radius (Jurac *et al.* 1998). More recoils produced closer to surface also deposit more electronic energy in the near surface region than in the case of the semi-infinite target. Therefore, the sputtering from the "sides" ("b" in Fig. 1) becomes the main contributor to the grain destruction. For larger incident energies, when the penetration depth is larger than a grain diameter, the ion completely penetrates the grain and causes sputtering on exiting the surface ("c" in Fig. 1). For example, for 100-keV O^+ ions, for which the sputtering rate peaks, the mean projected ion range (ion penetration depth projected to the incident ion direction) is ∼0.4 μm. Consequently, most of the 100-keV ions would completely penetrate through a 0.2-μm grain, resulting in a substantially increased sputtering rate.

The described transport code, calibrated to the measured yields for a flat surface (corresponding to the limit when grain radius goes to infinity), is applied here to grains in the micrometer and submicrometer ranges. In Fig. 5, we show the enhancement in the sputtering yield as a function of the incident ion energy for different grain sizes. The calculated yields, $Y(E, a) = \langle Y(E, a, \theta)\rangle_\theta$, are averaged over all incident angles, as in Eq. (1) for isotropic incidence, and normalized to the sputtering yield for a flat surface $Y(E, a, 0)$ at normal (0°) incidence.

The thick solid line represents the enhancement in the yield for isotropic incidence as plotted in Fig. 4. The symbols connected by a thin line correspond to different grain sizes (crosses, 1.6 μm; squares 0.8 μm; down triangles, 0.4 μm; up triangles, 0.1 μm;

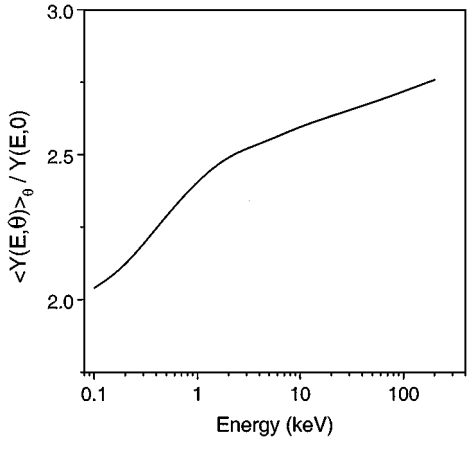

FIG. 4. Angle averaged sputtering yield on water–ice versus incident O ion energy normalized to the yield at normal incidence.

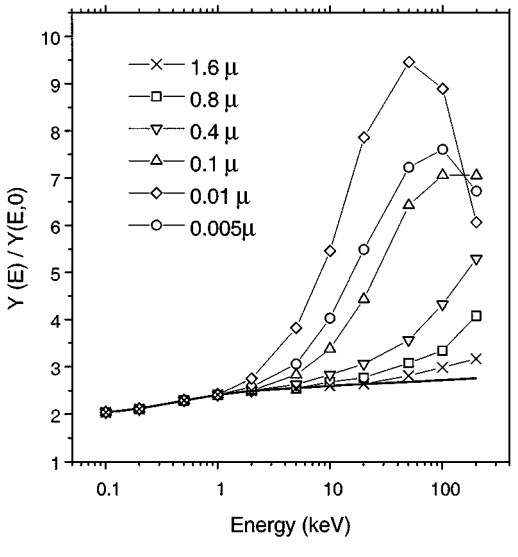

FIG. 5. Enhancement in the sputtering yield for ice grains as a function of the incident O ion energy, given for different grain sizes. Yields are averaged over all incident angles and normalized to the sputtering yield for flat surface at normal incidence.

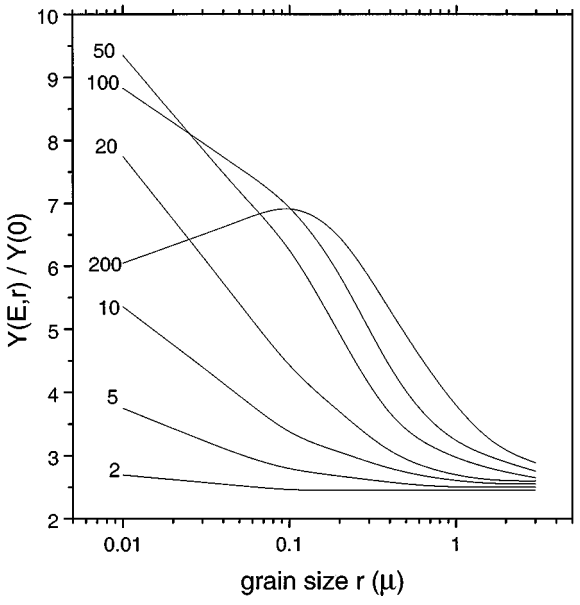

FIG. 6. Relative sputtering yield versus grain size for different incident ion energies in keV. Yields are averaged over all incident angles and normalized to the sputtering yield for a flat surface at normal incidence.

diamonds, 0.05 μm; circles, 0.01 μm). As seen in Fig. 5, for 50-keV O^+ ions impacting grains the yield increase as the grain size decreases; for a 1.6-μm grain the increase in yield due to the grain-size effect is less than 10%, for 0.4-μm grains it is about 50%, while for 0.1-μm grains it is almost a factor of 3. Grains larger than $\sim$2 μm can be treated as a semi-infinite target for energies below 200 keV. Another interesting feature displayed in Fig. 5, best seen for the smallest grains (0.05 μm, 0.01 μm), is that as the energy of the incident ion increases the relative yield goes through a maximum and decreases. This effect, previously observed in sputtering experiments on thin foils, results from the fact that, as the foil become much smaller than penetration depth of an ion, the total collisional energy deposited in the foil (and, consequently, the sputtering yield) starts to decrease. In this case, the incident ion zips through the grain (foil) without inducing a major collisional cascade. In Fig. 6, we replot the results from Fig. 5 as the relative sputtering yield versus grain size for different incident ion energies from 2 to 200 keV.

3. E-RING EROSION

The outgoing flux sputtered from a grain with radius a, presumed to be primarily H_2O for the temperatures of interest at Saturn, is calculated using

$$F_s(a) = \pi \int f(E, U)[Y(E, a) - 1]\Phi(E)\, dE, \qquad (2)$$

where $Y(E, a)$ represents the angle averaged sputtering yield $\langle Y(E, a)\rangle_\theta$ given in Fig. 4 and $\Phi(E)$ is the differential flux of incoming ions per steradian, which is assumed to be isotropic. For O^+, $\Phi(E)$ is obtained using a recent fit of an extended kappa distribution to the ion distribution at each satellite's radial distance (Jurac *et al.* 2001), while we interpolated values between satellites. Writing $[Y(E, a) - 1]$ in Eq. (2) accounts for the implanted incident particle. As seen in Fig. 2b, the energy at which the sputtering yield equals one is $\sim$60 eV implying that, if one ignores the incident H^+, there is no net mass flux to the surface. That is, for each incoming heavy ion one water molecule is sputtered from the surface. Below that energy incoming ions produce grain growth by implantation as the reflection probability is small. The factor $f(E, U) = [1 - \frac{eU}{E}]$, where U represents the grain potential and E is the ion energy in electron volts, accounts for the change in the geometrical cross section due to Coulomb attraction or repulsion. This factor is relevant only for energies $<$100 eV, since the estimated E-ring grain potential does not exceed $\pm$10 V. The corresponding effective impact energy E in $Y(E, a)$ for charged grains in Eq. (2) becomes $E - eU$.

For the E-ring grain potential we use values from Jurac *et al.* (1995), which are found to be consistent with the E-ring orbital dynamics simulation (Dikarev, 1999). Total sputter flux per unit grain area versus radial distance is given in Fig. 7. Beginning near Mimas, it is seen that sputter flux decreases, becomes nearly flat between Enceladus and Tethys, where most of the E-ring material is concentrated, and decreases further away. This flat region is where the higher energy plasma population is depleted due to absorption by ring particles as observed by Voyager LECP detectors.

After being sputtered from a grain, the ejected H_2O orbits Saturn (as H_2O, OH, or O) until ionization occurs. The energy distribution of neutrals sputtered from D_2O was measured by Riemann *et al.* (1984) and can be written as

$$F_e(E) = \frac{2U_s E}{(E + U_s)^3}, \qquad (3)$$

with $U_s = 0.055$ eV as an effective "binding energy" (Johnson, 1990). The average velocity of water-like neutrals given in

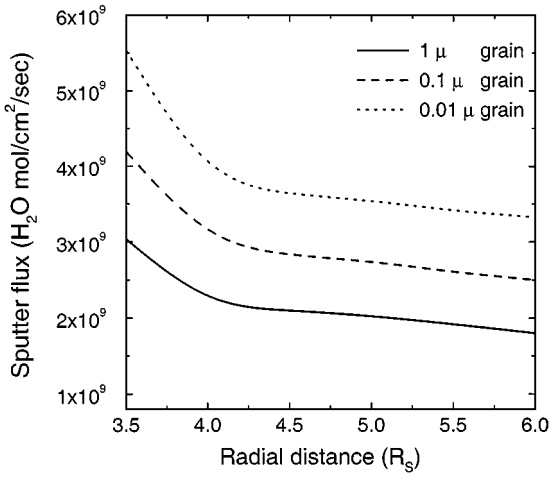

FIG. 7. Sputter flux from E-ring grains for different grain sizes versus radial distance in Saturn radii.

Eq. (3) corresponds to H_2O energies of ~0.5 eV. Since the neutral densities near Enceladus are in excess of 1000 cm^{-3} (Richardson *et al.* 1998), this "thermal" motion of the orbiting neutrals can lead to impact on E grains and, possibly, a grain growth (Johnson *et al.* 1989), a process that competes with sputtering. In addition to the "thermal speed" of water-like neutrals resulting from Eq. (3), grains move relative to the dense neutral cloud and sweep up the neutrals. The dynamics of smaller grains, if sufficiently charged, are affected by the Lorentz force. Very small grains with a high charge-to-mass ratio essentially behave like plasma particles corotating with the magnetic field (Burns *et al.* 1980). Assuming circular orbits, the relative grain velocity with respect to Keplerian velocity is given by Burns *et al.* (1984) as

$$\Delta v = \frac{q}{2m}\frac{B_0 R_s^3}{R^2}\left(1 - \frac{\omega}{\Omega}\right), \tag{4}$$

with Ω as the orbital angular velocity, ω the planet's spin rate, and B_0 as magnetic field at Saturn's surface $R = R_s$. As an example, in Fig. 8a we plot the grain velocity for different grain sizes at Enceladus' distance (3.95 R_s) for a grain potential of −5.5 V. Grains smaller than 0.1 μm are subject to acceleration by the Lorentz force while grains smaller than 0.01 μm develop a relative velocity larger than 10 km/s.

The calculated neutral accumulation on a grain, resulting from the flux determined using Eqs. (3) and (4), is given in Fig. 8b. It is seen that 0.01-μm grains, due to their substantially larger-than-Keplerian velocities, accumulate about four times more neutrals than larger (>0.1 μm) grains. However, the sputtered flux is always substantially larger than accumulated flux even in the most dense part of the neutral cloud. The eccentric orbits are expected to develop over time (Horanyi *et al.* 1992), implying non-uniform grain velocities that are not accounted for in Eq. (4). Although this will slightly influence the accumulated flux (Fig. 8b), an order of magnitude larger sputtered flux is seen in Fig. 7. We conclude that the accumulation of the neutrals cannot produce grain growth unless the average energy of the neutrals is seriously underestimated.

Based on light scattering observations, Showalter *et al.* (1991) modeled the normal optical depth of the E-ring as

$$\begin{aligned} \tau &= \tau_0\left(\frac{L}{3.95}\right)^{15} \quad \text{for} \quad L < 3.95 \\ \tau &= \tau_0\left(\frac{L}{3.95}\right)^{-7} \quad \text{for} \quad L > 3.95, \end{aligned} \tag{5}$$

with maximum optical depth at Enceladus (3.95 R_s) $\tau_0 = 1.5 \times 10^{-5}$ (see also Nicholson *et al.* 1996). For their assumed 1-μm grain size with $\rho = 1$ g/cm^3, the peak density is ~180 grains per square centimeter of the ring. Integrating the total net sputter flux over the surface area of the E ring as a function of radial distance L in Eq (5) gives a source rate 0.45×10^{26} H_2O molecules/s for the assumed uniform-size 1-μm E-ring grain population.

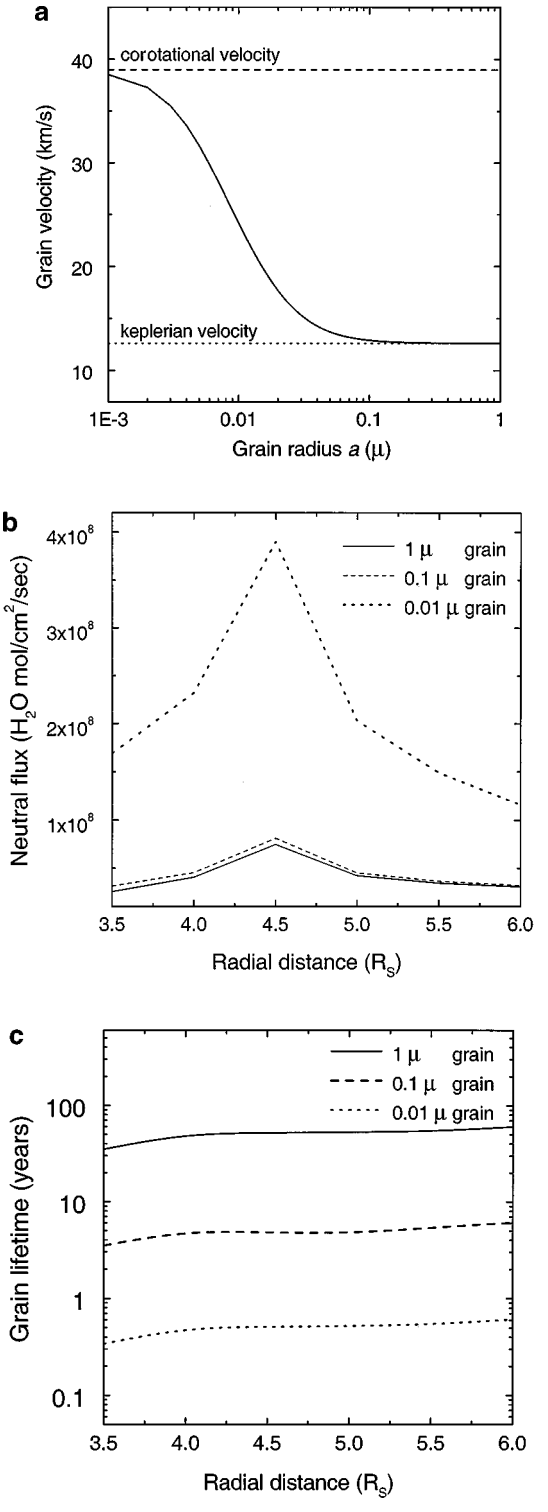

FIG. 8. (a) Grain velocity for different grain sizes at Enceladus' distance (3.95 R_s) for the grain potential of −5.5 V. Larger grains, like satellites, move with Keplerian velocity (dotted). Sufficiently small grains are picked up by magnetic field and corotate with the field lines (i.e., corotational velocity, dashed). (b) Accumulation of the neutral flux on a grain, a process that competes with sputtering. Very small grains (0.01 μm) accelerated by magnetic field "sweep" up neutrals. (c) Sputtering lifetimes for the E-ring grains at different radial distances (in Saturn radii).

Finally, in Fig. 8c we plot the lifetimes for different grain sizes based on the sputtering flux given in Fig. 7 and our model for enhanced sputtering of small grains (Figs. 5 and 6). It is important to note that this calculation gives only the lifetime against sputtering losses at a given radial distance. Over time, grains can attain eccentric orbits (Horanyi *et al.* 1992) and the total time spent at each radial distance should be taken into account to estimate the sputtering lifetime for a grain on a non-circular orbit. The lifetime of a 1-μm grain is about 50 years between Enceladus and Tethys, which is much shorter than previously estimated sputtering lifetimes (1000 years, Haff *et al.* 1983), while smaller grains disappear more rapidly: in years ($\sim$0.1 μm) or even months ($\sim$0.01 μm).

4. NEUTRAL CLOUD MODEL

H_2O molecules sputtered from the satellites and E-ring grains are ejected into the magnetosphere, forming a neutral cloud (Johnson *et al.* 1989). To obtain the resulting densities of water-group neutrals, we constructed an orbital simulation code which follows molecules in Saturn's gravity field. The initial velocities for the neutrals ejected from the orbiting satellites or E-ring particles were selected randomly, using the energy distribution given in Eq. (3).

The full, three-dimensional density of the E ring was used to describe the ring source. In addition to Eq. (5), we use the vertical thickness as a function of radial distance given by Showalter *et al.* (1991),

$$\sigma(L) = \frac{1}{8ln(2)} w_3 \left(\frac{w_8}{w_3}\right)^{(L-3)/5}, \qquad (6)$$

where $w_3 = 5900$ km represents the thickness at radial distance $L = 3R_s$. For the thickness at $L = 8R_s$, we use $w_3 = 18000$ km, based on the recent HST measurements of Nicholson *et al.* (1996). The source grains were randomly choosen on Keplerian orbits inside the E ring and each neutral in the simulation was emitted from a grain in a random direction. The submicrometer grains, which are presumably the principal source of plasma, are not expected to acquire significant eccentricity (contrary to 1-μm grain) as found by Horanyi *et al.* (1992) and Dikarev (1999). For instance, for a 0.5-μm grain with a sputtering lifetime of about 10 years the eccentricity would progress only to 0.05 (Dikarev 1999).

The heavy neutrals consist of H_2O, OH, and O molecules with different ionization lifetimes. The fraction of the population for each species was calculated locally by Richardson *et al.* (1998) as a function of the radial distance. The average lifetime of heavy neutrals was determined based on the lifetime and the fraction of each individual species.

The coordinates and velocity vector for each molecule were recorded at each time step until the molecule was lost from the population by ionization or by a collision with a satellite, main rings, or the E ring. As the moons were followed on their orbit, a neutral was considered lost when its path intersected the position of one of the moons. For neutrals crossing the main rings, a 0.9 collisional probability was assigned, while the probability for collision with E ring was based on this ring's local density. The spatial profile of heavy neutral lifetimes against ion-, electron-, and photo-induced ionization was based on the 2-D plasma model given by Richardson *et al.* (1998). Those lifetimes determine the survival probability at each time step in a Monte Carlo procedure. A typical time step of 10 min was needed, since the distance a neutral travels over a longer time step could move it to a region with a substantially different lifetime, especially when close to the equatorial plane. Beyond 12 R_s, rapid centrifugally driven transport of plasma begins and the underlying plasma model starts to break down (Richardson, 1998). Therefore, molecules straying beyond 15 R_s are excluded from our calculation and counted as lost. For simplicity, the collisional momentum transfer between corotating plasma ions and neutrals is not included here. The estimated collisional lifetime of OH near Enceladus is 178 days, compared to OH lifetime for ionization loss of about 80 days (Richardson 1998). Thus, while most OH is ionized before it is collisionally scattered, some small spreading of the neutral cloud will occur, which we do not yet account for in our simulation.

The calculation was performed until an equilibrium between source and loss rates was achieved, giving a steady-state neutral population. The resulting heavy-neutral densities are then recorded as a function of the radial distance from Saturn and the vertical distance from equatorial plane. The OH fraction of the water-like neutral population, given by Richardson *et al.* (1998) as a function of radial distance, was used to determine the resulting OH density, for comparison with the OH cloud derived from the HST observations.

Typically 50,000 particles were ejected from the E-ring and satellites randomly, one each time step, and followed over a period of 6–14 months until equilibrium was reached. The dominant loss mechanisms were ionization (90%), collision with main rings (5%), and escape beyond 15 R_S (4%), while collisions with the satellites and the E ring occurred less frequently ($<$1% of total losses).

5. RESULTS

Based on the calculated erosion rates, if the E ring is assumed to consist of 1-μ grains (Showalter *et al.* 1991), its source rate is at most 0.45×10^{26} H_2O molecules/s. The combined satellite sputtering sources estimated earlier gave $0.8–1\times10^{26}$ H_2O molecules/s (Jurac *et al.* 2001). The total production by satellites and E ring together is smaller than 1.5×10^{26} or about order of magnitude less than total source rate derived by Richardson *et al.* (1998) of 1.4×10^{27}. Although the calculated sputtering rates are affected by the uncertainties in plasma parameters and surface properties of the satellites (Jurac *et al.* 2001), this discrepancy is well beyond uncertainties in the calculated production rates.

The grain-size distribution produced by collisional disruption of ice yields the inverse power-law grain size distribution,

$$N(a)\,da = Ca^{-n}\,da, \tag{7}$$

where a is a grain radius and $N(a)\,da$ the number of particles between a and $a + da$ (Burns *et al.* 1984). The power index n for ice-on-ice experiments ranges from 2.9 to 3.7 (Kato *et al.* 1995, Arakawa 1999), essentially showing that collisions would produce much larger numbers of submicrometer-size than micrometer-size particles. For such values of n, smaller particles account for most of the surface area, while larger particles account for most of the mass. For the power size index $n > 3$, the scattering cross section is dominated by small particles, resulting in a reflected spectrum dominated by the blue wavelength (Throop and Esposito 1998). If the E-ring material is resupplied by collisions, either by the orbital collisions observed by Roddier *et al.* (1998) or by the Hamilton and Burns (1994) model, a significant submicrometer population should be introduced in the vicinity of Enceladus.

A uniform-size ($\sim$1 μm) E-ring population provided a better fit to the scattering observations (Showalter *et al.* 1991) than a power-law size distributions (Eq. (7)) with different indices n. Many possible distributions could satisfy the data (see, for instance, Throop and Esposito 1998, Burns *et al.* 1984). The preferential sputtering of small grains will modify an initial power-law distribution, which may significantly differ from the fits choosen by Showalter *et al.* (1991). Thus, the observed micro-signature in the Voyager 2 plasma data at Enceladus by Paranicas and Cheng (1997) may be *more* representative of the total surface area than the light-scattering observations. They found that 25 times the surface area of Enceladus is needed to account for the observed micro-signature in the Voyager data. The authors concluded that some of their assumptions might be incorrect, since such an object would certainly have been observed photometrically. We believe that the observed signature is mainly caused by a population of small grains orbiting at Enceladus' distance. As discussed later, the additional optically unobserved macroscopic material is also likely to be present as a source of those grains.

Assuming 25 times the Enceladus' surface area is in 1-μm (or larger) grains, the corresponding source rate is $\sim 5.3 \times 10^{26}$. This becomes 6.6×10^{26} for assumed 0.1-μm grains or 7.3×10^{26} molecules/s for 0.01-μm grains. This would bring the net sputter source to $6–8 \times 10^{26}$ molecules/s, still short of 14×10^{26} molecules/s required by Richardson *et al.* (1998), but within the range of uncertainty in the plasma model. Our estimate implies that for a source at the orbit of Enceladus about 50 times the surface area of Enceladus is needed to give the suggested 14×10^{26} molecules/s. To put additional constraints on the location of the H_2O sources, we explore the morphology of the neutral cloud resulted from our model and compare it with the cloud obtained from Hubble Space Telescope observations.

A number of simulation runs using satellites as the main plasma sources did not yield a cloud in agreement with the OH observations, so we conclude that even if the satellite sputtering is seriously underestimated, satellites alone could not produce the neutral/plasma torus observed in the Saturnian magnetosphere. The same conclusion is reached for the case of the micrometeorite bombardment of satellites as the possible source, since the radial distribution of the neutral cloud substantially deviates from that observed. On the other hand, the sharp peak of the E-ring density and the overall spatial structure indicate that either the E-ring is the dominant source, or that the neutral cloud and the E ring must have a common origin. Here we present two cases for which the closest fit to observations is obtained.

Figure 9a shows a contour plot of the resulting neutral cloud for the large E ring: the satellite sources (1×10^{26}) plus the E ring source, giving a total 1.4×10^{27} H_2O/s. Here the E ring is the dominant source of plasma with radial and vertical structure given by Eqs. (5) and (6), but with 25 times more surface area. In this hypothetical scenario we explore the possibility that a large population of "hidden" submicrometer grains is distributed throughout the E ring, which are not observed optically. Although the satellite sources are included here, they contribute little to the cloud structure. The general morphology of the cloud (Fig. 9a) is similar to that of the cloud derived by Richardson *et al.* (1998), shown in Fig. 9c. Due to the plasma-neutral collisions, not accounted for in our cloud model, the lower density contours at larger radial distances from Saturn ($L > 6$) are subject to more uncertainties than at the higher densities for $L < 6$. Besides the exact position of the peak density, the main difference between Fig. 9a and Fig. 9b is that the high-density contours are more concentrated near the equatorial plane than those given by Richardson *et al.* (1998) (Fig. 9c).

Figure 9b shows the combined neutral densities for the satellite sources (1×10^{26}) plus the "regular" E-ring source (0.5×10^{26}) and, an additional large source near Enceladus' orbit, all totaling 1.4×10^{27} H_2O/s. That is, we assume a large source near Enceladus, approximately 50 times its surface area contained in small grains (0.1 μm). The morphology of the resulting OH cloud closely resembles the morphology of the OH cloud derived from HST observations (Richardson *et al.* 1998), especially for the high-density contours. This suggests that the missing source is likely located near Enceladus rather than spread over the whole E ring. As a result we conclude that a large (of the order 10^{27} H_2O/s), *concentrated* source is needed near the orbit of Enceladus.

This cloud (Fig. 9b) is characterized by high densities (with maximum approaching 800 cm^{-3}) extending verticaly above the equatorial plane. The peak density is at 4 R_s, while the cloud found by Richardson *et al.* (1998) peaks at about 4.5 R_s. However, the neutral cloud densities were measured by HST only at distances of 2, 4.5, 6, and 10 R_s, leaving the exact position of the peak density uncertain. The outward drift of submicrometer grains, which develops over time, may also contribute to the shift of the peak density toward Tethys. Dikarev (1999) estimated that the most rapidly drifting grains considered, 0.1 μm (smaller grains exceeded the accuracy of the method used), can cross the

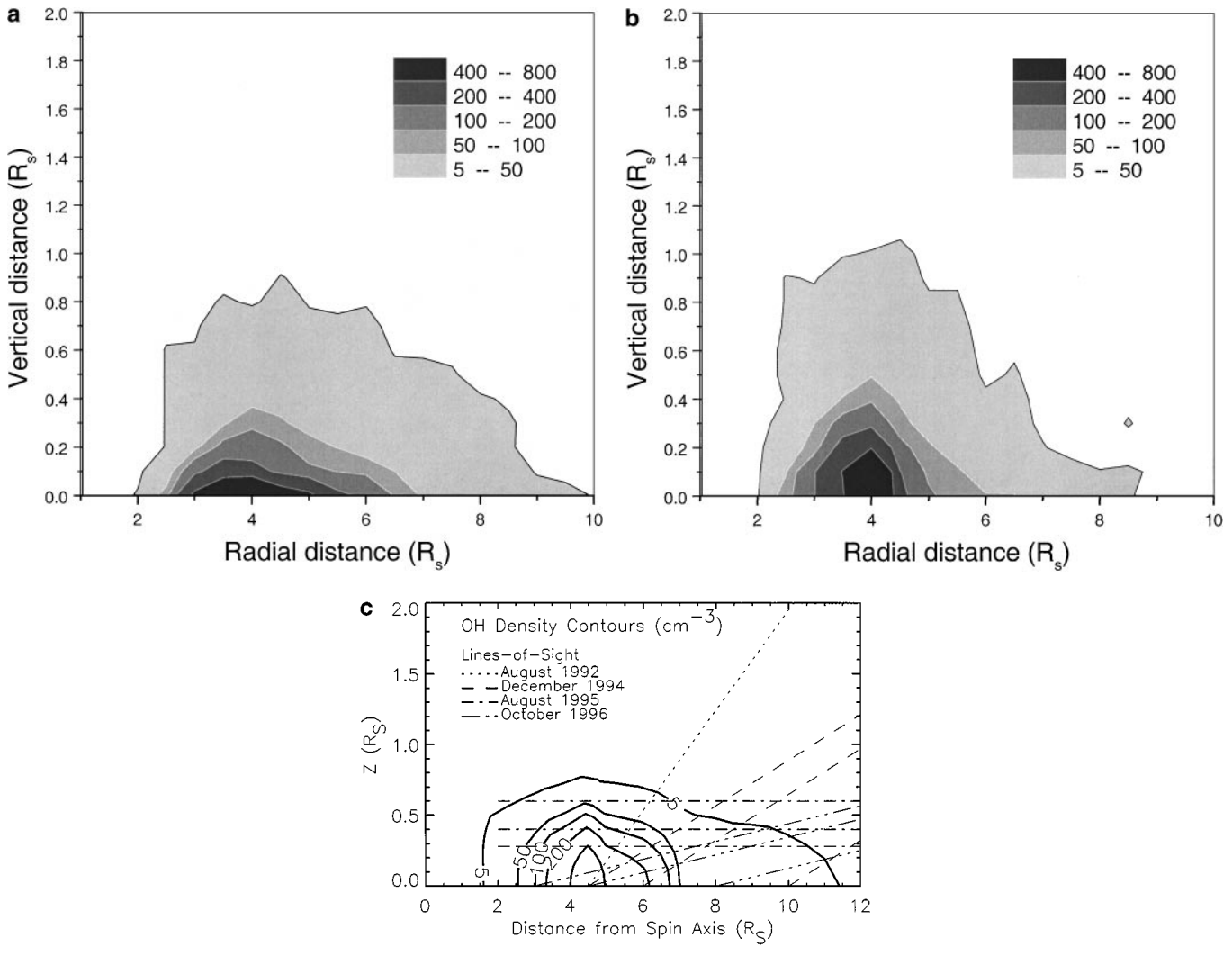

FIG. 9. (a) Neutral cloud for a large E-ring source distributed through E ring. OH densities for the satellite sources (1×10^{26} H_2O molecules/s) plus a large E-ring source, both totaling 1.4×10^{27}. (b) Neutral cloud for a large source concentrated near Enceladus. OH densities for the satellite sources (1×10^{26} H_2O molecules/s) plus E-ring source (0.5×10^{26}) plus a large source near Enceladus (1.25×10^{27}), which is about 50 times Enceladus' surface area. Total source rate is 1.4×10^{27}, equal to that in Figs. 9a and 9c for comparison. (c) Neutral OH cloud derived by Richardson *et al.* (1998), based on Hubble Space Telsecope observations with lines-of-sight shown.

E ring in about 15 years, while their sputtering lifetime is about 2 years (Fig. 8c). Consequently, the submicrometer grains are sputtered fast, and their contribution to the neutral cloud should remain localized between Enceladus and Tethys.

6. DISCUSSION

The orbital simulations presented here show that a large source of H_2O neutrals is needed near Enceladus to explain the measured OH densities (Richardson *et al.* 1998). A number of other peculiarities associated with the E ring show that there are significant gaps in the present understanding of that region. Carbary *et al.* (1983) reported a "true anomaly" in the plasma micro-signature measured by Voyager 2: no signature was observed when the spacecraft was in the plasma wake downstream of Enceladus but a strong signature was present in all electron and ion channels upstream. They suggested that "clumping" of the E-ring material might be responsible for the observed phenomenon. Paranicas and Cheng (1997) concluded that about 25 times the absorbing area of Enceladus is needed between Enceladus and its Lagrangian L_5 point to account for the observed ion micro-signature. Only a marginal optical evidence of additional material near the L_5 point was reported by Baum *et al.* (1981).

This optically unseen "absorbing area" for ions is an effective source of neutrals, since these ions missing from the local population will sputter away a large amount of H_2O neutrals when impacting icy material. If the sputtering is the principal mechanism for H_2O re-supply, then the surface area of the E ring must be more than an order of magnitude larger than that inferred from the optical observations. The surface area estimated from

light scattering observations (Showalter *et al.* 1991, Nicholson *et al.* 1996) is based on the assumption that the E ring consists of a narrow-size 1-μm grain population. For purpose of modeling those observations, a guess should be made about a grain-size distribution, and many possible distributions could satisfy the data (see review by Burns *et al.* 1984). Also, the optical observations are insensitive to the grains smaller than 0.1 μm, which scatter light inefficiently.

We propose that a large population of submicrometer grains near Enceladus could resolve the discrepancy between optical and plasma observations. As discussed earlier, submicrometer grains have short lifetimes and must be replenished frequently. If the E ring is the principal source of plasma, what possible mechanism could be responsible for re-supplying E-ring grains?

Hamilton and Burns (1994) proposed a model in which the E ring is self-sustained by grain collisions with Enceladus. In their model, micrometer-size grains are driven to eccentric orbits by the Lorentz force and solar radiation pressure, colliding with the surfaces of icy moons and ejecting new grains. These hypervelocity collisions also evaporate some material, likely ejecting H_2O from the satellites and main rings (Ip 1997). Ice-on-ice collision experiments (Kato *et al.* 1995, Arakawa 1999) have yet to determine the efficiency of this production from grainy and porous surfaces, and the fraction of produced H_2O that would escape from the satellites. However, the grain–moon collisions would produce a large number of submicrometer grains, which we have shown are preferentially depleted by sputtering. Thus, the power-law grain distribution expected to result from collisions would be driven toward a narrow-size distribution, in better agreement with the observations by Showalter *et al.* (1991). The sputter erosion of grains will also impact the orbital dynamics of the grains, which is very sensitive to the grain radius. Without a new orbital simulation, which includes mass loss over time, it is hard to speculate on the further implications that small grain erosion would have on the proposed model.

We suggest an alternative explanation to the Hamilton and Burns (1994) model: mutual collisions of icy fragments near Enceladus, possibly remains of a satellite at the L_5 point that was previously broken apart and subsequently fragmented. Smaller ($\sim$15 km) bodies exist near the Lagrangian points of two other near-by satellites: Telesto at L_4 and Calypso at L_5 near Tethys, and Helene at L_5 around Dione. If a similar object was present around Enceladus, and was consequently disrupted, a large number of smaller bodies would be present. A similar scenario was proposed earlier for the G ring: the largest remaining fragments from the initial disruption become G-ring parent bodies, which act as sources for the observed dust ring (Showalter and Cuzzi 1993, Canup and Esposito 1997). Most of the mass would be contained in larger (meter to $\sim$kilometer size) objects, while most of the surface area would be contained in smaller grains. We suggest that the grains are re-supplied by orbital collisions between large icy fragments, and simulteneously sputtered away, forming the neutral/plasma population. Once a large fragment is futher broken apart by a hard collision, an initial power-law grain-size distribution is formed. The tiniest grains ($\ll$0.1 μm) are small enough to be picked up and accelerated to the corotational speed and remain in the neighborhood of Enceladus' orbit (Dikarev 1999). These grains move several times faster than the Keplerian speed, thus frequently colliding with larger fragments and contributing to their further erosion.

A recent observation of a bright arc around Enceladus by Roddier *et al.* (1998) provides support for this scenario. Authors argue that the observed arc consists of small ($\sim$1 μm) particles produced by an orbital collision. Based on the observed slight inclination of the arc (1.8 degree) and its orbital radius, which is larger than Enceladus' (242,600 instead of 238,000 km), Roddier *et al.* (1998) speculated that a large ice block collided with ice fragments trapped near the L_4 Lagrangian point. This collision, observed by chance, was bright enough to be noticed. If the macroscopic material near Enceladus's orbit was produced by a catastrophic disruption as we suggest (i.e., follows a power-law size distribution, with the predominace of smaller bodies), a larger number of smaller collisions are likely occurring and remain unnoticed.

From the rapid disappearance of the arc, Roddier *et al.* (1998) concluded that the particles evaporated. Since any evaporation would have likely occurred immediately after the impact, we believe that a large amount of submicrometer particles was released in that collision. They became negatively charged by the surrounding low-energy electrons (Jurac *et al.* 1995) and quickly re-distributed by the corotating magnetic field. The brightness of the arc decayed to about one-half of its original brightness during one hour of observations. The amount of extra electrons necessary to develop a typical grain potential of -5 V around Enceladus is collected in about 20 min (Dikarev 1999), putting it on the same time scale as the arc's dissapearance. As shown in Fig. 8a, depending on their size, the charged submicrometer grains would acquire different orbital velocities, and the feature would appear to fade away due to the spreading of the material.

7. CONCLUSION

In this article, we created a detailed model of the sputtering of small ice grains by energetic plasma ions to examine the sputtering effect on the E-ring grain population. We showed that the E-ring grain erosion occurs much faster than previously estimated, in about 50 years for 1-μm grains compared to previous estimates of 10^3 years (Haff *et al.* 1983) and 6×10^3 years (Morfill *et al.* 1983). This result places tight constraints on the orbital-dynamics calculations of the grain motion, as the grains are typically followed for hundreds of years when describing the evolution of the E ring. This result also shows that grains must be re-supplied much faster than previously thought to maintain the E ring.

An orbital simulation model of the evolution of H_2O molecules emitted from the satellites and the E ring, although not fully self-consistent, is employed to place constraints on the possible plasma/neutral sources in Saturn's magnetosphere. We

concluded that an additional large source concentrated near the orbit of Enceladus is needed to account for the observed OH neutral cloud. We showed that a surface area 25 times larger than Enceladus, as implied by energetic particle signatures near the orbit of Enceladus (Paranicas and Cheng 1997), would produce more than half of the neutrals needed. Since the plasma micro-signature is most sensitive to the material in the spacecraft vicinity, it is possible that the actual amount of the absorbing area spread over the ring region is larger than that detected in a single Voyager pass. We estimate that about 30–60 times of the Enceladus' surface area, depending on the grain size chosen, is needed to account for the neutral production rate of 1.4×10^{27} H_2O/s derived by Richardson *et al*. (1998). A source of these grains, as argued earlier, may be the icy fragments near the orbit of Enceladus (likely contained around Lagrangian points), possibly remains of a disrupted satellite. Orbital collisions between those fragments of ice are suggested as the production mechanism for a large submicrometer grain population needed as a source.

If these orbital collisions were the ultimate source of the neutral cloud and plasma, as argued here, time variations in the plasma and grain densities may be expected. In fact, time variations in plasma densities may be the reason for the difficulty in obtaining self-consistency between sputter sources and the neutral and plasma torus observations. Based on the likelihood that additional unobserved macroscopic material might be present near Enceladus' Lagrangian points, we suggest that the Cassini spacecraft should remotely explore that region prior to making a close pass through it.

ACKNOWLEDGMENTS

This work is supported by the the Origins and the Geology and Geophysics programs of NASA at UVA, by the NSF Astronomy program at UVA, and by NASA Planetary Atmospheres Grant NAGW 5-6129 at MIT.

REFERENCES

Arakawa, M. 1999. Collisional distribution of ice by high-velocity impact. *Icarus* **142**, 34–45.

Baum, W. A., T. Kreidl, J. A. Westphall, G. E. Danielson, P. K. Seidelmann, D. Pascu, and D. G. Currie 1981. Saturn's E Ring. *Icarus* **47**, 84–96.

Bringa, E., R. E. Johnson, and L. Dutkiewicz 1999a. Molecular dynamics study of non-equilibrium energy transport from a cylindrical track: II Spike models for sputtering yield. *Nucl. Instrum. Methods B* **152**, 267–290.

Bringa, E., R. E. Johnson, and M. Jakas 1999b. Molecular dynamics simulations of electronics sputtering. *Phys. Rev.* **60**, 15107–15116.

Brown, W. M., Augustyniak, K. J. Marcantonio, E. Simmons, J. W. Boring, R. E. Johnson, and C. T. Reimann 1984. Electronic sputtering of low temperature molecular solids. *Nucl. Instrum. Methods* **B1**, 307–314.

Brown, W. L., W. M. Augustyniak, E. Simmons, K. J. Marcantonio, L. J. Lanzerotti, R. E. Johnson, J. W. Boring, C. T. Reimann, G. Foti, and V. Pirronello 1982. Erosion and molecular formation in condensed gas films by electronic energy loss of fast ions. *Nucl. Instrum. Methods* **198**, 1–8.

Burns, J. A., M. R. Showalter, J. N. Cuzzi, and J. B. Pollack 1980. Physical processes in Jupiter's ring: Clues to its origin by Jove! *Icarus* **44**, 339–360.

Burns, J. A., M. R. Showalter, and G. E. Morfill 1984. The ethereal rings of Jupiter and Saturn. In *Planetary Rings* (R. Greenberg and A. Brahic, Ed.), p. 21–56. Univ. of Arizona Press, Tucson.

Canup, R., and L. Esposito 1997. Evolution of the G ring and the population of macroscopic ring particles. *Icarus* **126**, 28–41.

Carbary, J. F., S. M. Krimigis, and W.-H. Ip 1983. Energetic particle microsignatures of Saturn's satellites. *J. Geophys. Res.* **88**, 8947–8958.

Cheng, A. F., and L. J. Lanzerotti 1978. Ice sputtering by radiation belt protons and the rings of Saturn and Uranus. *J. Geophys. Res.* **83**, 2579–2602.

Dikarev, V. V. 1999. Dynamics of particles in Saturn's E-ring: Effects of charge variations and the plasma drag force. *Astron. Astrophys.* **346**, 1011–1019.

Eckstein, W. 1991. *Computer Simulation of Ion–Solid Interactions*. Springer, Berlin.

Eviatar, A. 1984. Plasma in Saturn's magnetosphere. *J. Geophys. Res.* **89**, 3821–3828.

Gan-Baruch, Z., A. Eviatar, J. D. Richardson, and R. L. McNutt, Jr. 1994. Plasma observations in the ring plane of Saturn. *J. Geophys. Res.* **99**, 11063–11077.

Haff, P. K., A. Eviatar, and G. Siscoe 1983. Ring and plasma: The enigmae of Enceladus. *Icarus* **56**, 426–439.

Hall, D. T., P. D. Feldman, J. B. Holberg, and M. A. McGrath 1996. Fluorescent hydroxyl emissions from Saturn's ring atmosphere. *Science* **272**, 516–518.

Hamilton, D. P., and J. A. Burns 1994. Origin of Saturn's E ring: Self sustained, naturally. *Science* **264**, 550–553.

Hamilton, D. P., and J. A. Burns 1993. OH in Saturn's rings, *Nature* **365**, 498–498.

Horanyi, M., J. A. Burns, and D. P. Hamilton 1992. The dynamics of Saturn's E ring particles. *Icarus* **97**, 248–259.

Ip, W.-H. 1997. On neutral cloud distributions in the saturnian magnetosphere. *Icarus* **126**, 42–57.

Johnson, R. E. 1990. *Energetic Charged-Particle Interactions with Atmospheres and Surfaces*. Springer-Verlag, Berlin.

Johnson, R. E., L. J. Lanzerotti, and W. L. Brown 1984. Sputtering processes: Erosion and chemical change. *Adv. Space Res.* **4**, 41–51.

Johnson, R. E., M. K. Pospieszalska, E. C. Sittler, A. F. Cheng, L. J. Lanzerotti, and E. M. Sievka 1989. The neutral cloud and heavy ion inner torus at Saturn. *Icarus* **77**, 311–329.

Jurac, S., R. A. Baragiola, R. E. Johnson, and E. C. Sittler 1995. Charging of ice grains by low energy plasmas: Application to Saturn's E ring. *J. Geophys. Res.* **100**, 14821–14831.

Jurac, S., R. E. Johnson, and B. Donn 1998. Monte Carlo calculations of the sputtering of grains: Enhanced sputtering of small grains. *Astrophys. J.* **503**, 247–252.

Jurac, S., R. E. Johnson, J. D. Richardson, and C. Paranicas 2001. Satellite sputtering in Saturn's magnetosphere. accepted in *Planet. Space Sci.*

Kato, M., Y. Iijima, M. Arakawa, Y. Okimura, A. Fujimura, N. Maeno, and H. Mizutani 1995. Ice on ice experiments. *Icarus* **113**, 423–441.

Krimings, S. M., J. F. Carbary, E. P. Keath, T. P. Armstrong, L. J. Lanzerotti, and G. Gloeckler 1983. General characteristic of hot plasma and energetic particles in the saturnian magnetosphere: Results from the Voyager spacecraft. *J. Geophys. Res.* **88**, 8871–8892.

Lanzerotti, L. J., C. G. Maclennan, W. L. Brown, R. E. Johnson, L. A. Barton, C. T. Reiman, J. W. Garrett, and J. W. Boring 1983. Implication of Voyager data for energetic ion erosion of the icy satellites of Saturn. *J. Geophys. Res.* **88**, 8765–8770.

Lazarus, A., and R. McNutt, Jr. 1983. Low-energy plasma ion observations in Saturn's magnetosphere. *J. Geophys. Res.* **88**, 8831–8846.

Meyer-Vernet, N., A. Lecheux, and B. M. Pedersen 1996. Constraints on Saturn's E-ring from the Voyager 1 radio astronomy instrument. *Icarus* **123**, 113–128.

Morfill, G. E., O. Havens, and C. K. Goertz 1993. Origin and maintenance of the oxygen torus in Saturn's magnetosphere. *J. Geophys. Res.* **98**, 11285–11298.

Nicholson, P. D., M. Showalter, L. Dones, R. G. French, S. M. Larson, J. J. Lissauer, C. A. McGhee, P. Seitzer, B. Siscardy, and G. E. Danielson 1996. Observations of Saturn's ring-plane crossings in August and November 1995. *Science* **272**, 509–515.

Pang, K. D., C. C. Voge, J. W. Rhoads, and J. M. Ajello 1984. The E-ring of saturn and satellite Enceladus. *J. Geophys. Res.* **89**, 9459–9470.

Paranicas, C., and A. F. Cheng 1997. A model of satellite microsignatures for Saturn. *Icarus* **125**, 380–396.

Pater, I., M. R. Showalter, J. J. Lissauer, and J. R. Graham 1996. Keck infrared observations of Saturn's E and G rings during Earth's 1995 ring plane crossings. *Icarus* **121**, 195–198.

Pospieszalska, M. K., and R. E. Johnson 1991. Micrometeorite erosion of the main rings as a source of plasma in the inner saturnian plasma torus. *Icarus* **93**, 45–52.

Richardson, J. D. 1998. Thermal plasma and neutral gas in Saturn's magnetosphere. *Rev. Geophys.* **36**, 501–524.

Richardson, J. D., A. Eviatar, M. A. McGrath, and V. M. Vasyliunas 1998. OH in Saturn's magnetosphere: Observations and implications. *J. Geophys. Res.* **103**, 20245–20255.

Richardson J. D, and E. C. Sittler, Jr. 1990. A plasma density model for Saturn based on Voyager observations. *J. Geophys. Res.* **95**, 12019–12031.

Riemann, C. T., J. W. Boring, R. E. Johnson, J. W. Garrett, K. R. Farmer, and W. L. Brown 1984. Ion-induced molecular ejection from D_2O ice. *Surf. Sci.* **147**, 227–240.

Roddier, C., F. Roddier, J. E. Graves, and M. J. Northcott 1998. Discovery of an arc of particles near Enceladus' orbit: A possible key to the origin of the E-ring. *Icarus* **136**, 50–59.

Shemansky, D. E., and D. T. Hall 1992. The distribution of atomic hydrogen in the magnetosphere of Saturn. *J. Geophys. Res.* **97**, 4143–4161.

Shemansky, D. E., P. Matherson, D. T. Hall, H.-Y Hu, and T. M. Tripp 1993. Detection of the hydroxyl radical in the Saturn magnetosphere. *Nature* **363**, 329–332.

Shi, M., R. A. Baragiola, D. E. Grosjean, R. E. Johnson, S. Jurac, and J. Schou 1995. Sputtering of water ice surfaces and the production of extended neutral atmospheres. *J. Geophys. Res.* **100**, 26387–26395.

Showalter, M. R., and J. N. Cuzzi 1993. Seeing ghosts: Photometry of Saturn's G ring. *Icarus* **103**, 124–143.

Showalter, M. R., J. N. Cuzzi, and S. M. Larson 1991. Structure and particle properties of Saturn's E ring. *Icarus* **94**, 451–473.

Throop, H. B., and L. W. Esposito 1998. G ring particle sizes derived from ring plane crossing observations. *Icarus* **131**, 152–166.

Tsintikidis, D., D. Gurnett, L. J. Granroth, S. C. Allendorf, and W. S. Kurth 1994. A revised analysis of micron-sized particles detected near Saturn by the Voyager 2 plasma wave instrument. *J. Geophys. Res.* **99**, 2261–2270.

Tsintikidis, D., W. S. Kurth, D. A. Gurnett, and D. D. Barbosa 1995. Study of dust in the vicinity of Dione using the Voyager 1 plasma wave instrument. *J. Geophys. Res.* **100**, 1811–1822.

Ziegler, J. F., J. P. Biersack, and U. Littmark 1985. *The Stopping and Ranges of Ions in Solid*. Pergamon, New York.